Nonlinear evolution of resistive tearing mode instability with shear flow and viscosity

L. Ofman[a] and P. J. Morrison
Department of Physics and Institute for Fusion Studies, The University of Texas at Austin, Austin, Texas 78712

R. S. Steinolfson
Department of Space Sciences, Southwest Research Institute, San Antonio, Texas 78228

(Received 25 March 1992; accepted for publication 2 October 1992)

The nonlinear evolution of the tearing mode instability with equilibrium shear flow is investigated via numerical solutions of the resistive magnetohydrodynamic (MHD) equations. The two-dimensional simulations are in slab geometry, are periodic in the x direction, and are initiated with solutions of the linearized MHD equations. The magnetic Reynolds number S was varied from 10^2 to 10^5, a parameter V that measures the strength of the flow in units of the average Alfvén speed was varied from 0 to 0.5, and the viscosity as measured by the Reynolds number S_ν satisfied $S_\nu > 10^3$. When the shear flow is small ($V < 0.3$) the tearing mode saturates within one resistive time, while for larger flows the nonlinear saturation develops on a longer time scale. The two-dimensional spatial structure of both the flux function and the streamfunction distort in the direction of the equilibrium flow. The magnetic energy release decreases and the saturation time increases with V for both small and large resistivity. Shear flow decreases the saturated magnetic island width, and generates currents far from the tearing layer. The validity of the numerical solutions was tested by verifying that the total energy and the magnetic helicity are conserved. The results of the present study suggest that equilibrium shear flow may improve the confinment of tokamak plasma.

I. INTRODUCTION

The resistive tearing instability is an important phenomenon in laboratory and space plasma and was first studied in its linear regime by Furth *et al.*[1] The instability grows in a narrow layer of the plasma where the resistivity term dominates the local magnetic field term in Ohm's law and thereby allows the field lines to tear or reconnect and form magnetic islands. The linear growth rate of the tearing mode scales as $S^{-3/5}$ where S is the magnetic Reynolds number (defined below).

Large shear flows have been observed between the magnetic footpoints of solar flares as well as along field lines[2] where tearing and reconnection may occur.[3] The analytic linear theory of the tearing mode with equilibrium shear flow and viscosity has been considered by several authors.[4–8] These studies conclude that flows approaching the Alfvén velocity can greatly modify the stability criteria of the tearing instability. This was also shown to hold numerically in the linear regime for the tearing mode.[9–12]

Nonlinear saturation of the tearing mode without flow occurs within one or several growth times, and the growth slows from exponential to algebraic.[13] Numerical evolution of the nonlinear tearing mode (without flow) in slab geometry was studied by Schnack[14] and Schnack and Killeen[15] using the finite-difference alternative-direction implicit (ADI) approach. The energetics, growth rate, and spatial behavior for several values of resistivity and for both constant-ψ and nonconstant-ψ regimes of the tearing mode without flow were investigated by Steinolfson and Van Hoven.[16]

The effect of plasma rotation on the nonlinear tearing mode was considered recently by Persson and Bondeson[17] and Persson.[18,19] They solved the reduced magnetohydrodynamic (MHD) equations with the spectral approach using up to seven modes, and found that when flow is sufficiently strong, the viscosity sufficiently small, and only the $m=2/n=1$ and $m=4/n=2$ modes are present, the nonlinear evolution of the tearing mode can lead to nonlinear oscillatory behavior. A single value of the magnetic Reynolds number ($S=10^6$) was used in their studies. These nonlinear oscillations were obtained analytically by Chen and Morrison[20] using center manifold reduction.

The effect of shear flow on the nonlinear evolution of the tearing mode is investigated numerically in the present study via solution of the incompressible two-dimensional resistive MHD equations in slab geometry (rather than reduced MHD equations) using the finite-difference ADI method. The nonlinear tearing mode (without shear flow) studies by Steinolfson and Van Hoven[16] are extended to include the effects of shear flow. The work of Persson[18,19] and Persson and Bondeson[17] is extended to include the higher resistivity range with values of the magnetic Reynolds number $10^2 \leqslant S \leqslant 10^5$. The finite difference approach in this work is not limited to the small number of modes used in the previous works and enables us to study the effect of shear flow on the energy distribution, the energy dissipation, and the nonlinear growth rate of the tearing mode.

This is a first study of the effect of both symmetric and

[a]Present address: NASA Goddard Space Flight Center, Code 682.1, Greenbelt, Maryland 20771.

 0899-8221/93/020376-12$06.00

antisymmetric (with respect to the resonant magnetic surface) shear flow profiles on the nonlinear energy release, and on the saturated magnetic island width of the tearing mode for wide parameter range. This is also a first study of the effect of the shear flow on the nonlinear growth rates and energy dissipation. We find that the presence of equilibrium shear flow can reduce the amount of magnetic energy release, increase the saturation time (reduce the nonlinear growth rate), and reduce the saturated magnetic island width. The nonlinear saturation of the tearing mode with shear flow in the higher resistivity and viscosity range ($S<10^5, S_\nu>10^3$) is generally monotonic in time, and no sustained nonlinear oscillations are found in our studies.

The paper is organized as follows: In Sec. II the nonlinear MHD equations in slab geometry, the initial magnetic field configuration, the equilibrium flow profiles, and the relevant conservation relations are presented. In Sec. III we present the numerical method of solution. Section IV is devoted to the numerical results, and a summary is given in Sec. V.

II. MHD EQUATIONS

We assume that collisional MHD theory is applicable,[21] that the plasma is incompressible with constant isotropic resistivity η and constant perpendicular viscosity ν,[22] and that gravitational effects are negligible. The basic equations in cgs units are

$$\rho\left(\frac{\partial \mathbf{v}}{\partial t}+(\mathbf{v}\cdot\nabla)\mathbf{v}\right)=-\nabla P+\frac{1}{4\pi}(\nabla\times\mathbf{B})\times\mathbf{B}+\rho\nu\nabla_\perp^2\mathbf{v}, \tag{1}$$

$$\frac{\partial \mathbf{B}}{\partial t}=\nabla\times(\mathbf{v}\times\mathbf{B})-\frac{c^2\eta}{4\pi}\nabla\times(\nabla\times\mathbf{B}), \tag{2}$$

$$\nabla\cdot\mathbf{v}=0, \quad \nabla\cdot\mathbf{B}=0, \tag{3}$$

where c is the speed of light, ρ is the constant plasma density, $\mathbf{B}$ is the magnetic field, $\mathbf{v}$ is the plasma velocity, and P is the plasma pressure. We use Cartesian geometry (with unit vectors $\mathbf{e}_x$, $\mathbf{e}_y$, and $\mathbf{e}_z$) and choose equilibrium magnetic and velocity fields of the form

$$\mathbf{B}=B_0(y)\mathbf{e}_x+\nabla_\perp\psi\times\mathbf{e}_z\equiv\nabla_\perp\Psi\times\mathbf{e}_z, \tag{4}$$

$$\mathbf{v}=v_0(y)\mathbf{e}_x+\nabla_\perp\phi\times\mathbf{e}_z\equiv\nabla_\perp\Phi\times\mathbf{e}_z, \tag{5}$$

where Ψ and Φ are the total flux function and streamfunction, and ψ and ϕ are the flux function and streamfunction relative to the equilibrium quantities B_0 and v_0.

Substituting Eqs. (4) and (5) in Eqs. (1)–(3), taking the curl of Eq. (1), thus eliminating the pressure P, and considering the $\mathbf{e}_x-\mathbf{e}_y$ components in dimensionless form gives the following 2-D (two-dimensional) MHD equations

$$\frac{\partial\psi}{\partial t}=-\left(\frac{\partial\phi}{\partial y}+G\right)\frac{\partial\psi}{\partial x}+\left(\frac{\partial\psi}{\partial y}+F\right)\frac{\partial\phi}{\partial x}+\frac{1}{S}\nabla_\perp^2\psi, \tag{6}$$

$$\frac{\partial(\nabla_\perp^2\phi)}{\partial t}=-\left(\frac{\partial\phi}{\partial y}+G\right)\frac{\partial(\nabla_\perp^2\phi)}{\partial x}+\frac{\partial\phi}{\partial x}\left(\frac{d^2G}{dy^2}+\frac{\partial(\nabla_\perp^2\phi)}{\partial y}\right)+\left(\frac{\partial\psi}{\partial y}+F\right)\frac{\partial(\nabla_\perp^2\psi)}{\partial x}-\frac{\partial\psi}{\partial x}\left(\frac{d^2F}{dy^2}+\frac{\partial(\nabla_\perp^2\psi)}{\partial y}\right)+\frac{1}{S_\nu}\nabla_\perp^4\phi, \tag{7}$$

where $\nabla_\perp^2\equiv\partial^2/\partial x^2+\partial^2/\partial y^2$ and $\partial/\partial z=0$. We have also assumed that the equilibrium magnetic field is maintained by an external electric field, and we imagine that the equilibrium flow is similarly maintained. The coordinates are referenced to the magnetic shear length scale a_b, the time to the Alfvén time τ_h (given below), and magnetic field to $B=|\mathbf{B}_0(y_{\max})|$, where $y_{\max}$ is the distance from the tearing layer to the y boundary.

The dimensionless parameters are the magnetic Reynolds number $S=\tau_r/\tau_h$, the viscous Reynolds number $S_\nu=\tau_\nu/\tau_h$, and the shear parameter $R=a_b/a_v$, where a_v is the velocity shear length scale. The relevant time scales in these definitions are the resistive time τ_r, the Alfvén time τ_h, and the viscous time τ_v given by

$$\tau_h=\frac{a_b(4\pi\rho)^{1/2}}{B}, \quad \tau_r=\frac{4\pi a_b^2}{c^2\eta}, \quad \tau_\nu=\frac{\rho a_b^2}{\nu}.$$

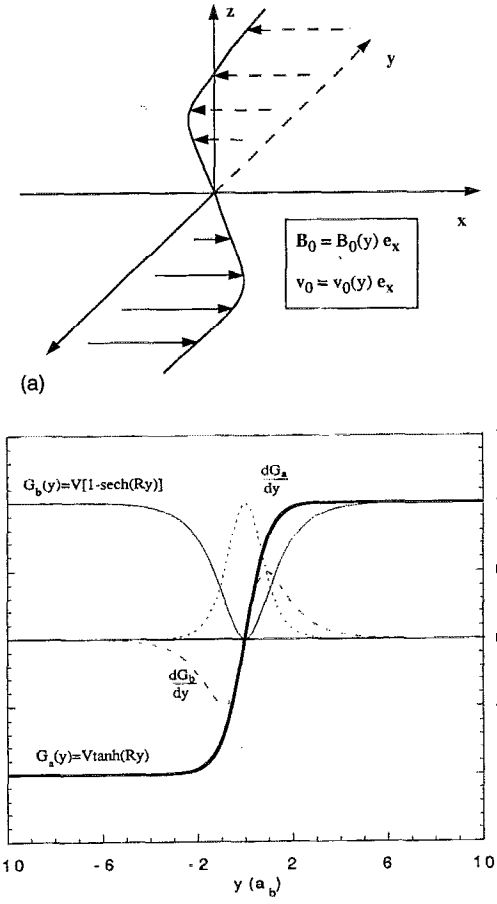

FIG. 1. The initial equilibrium magnetic field and flow. (a) The tanh dependence on y of $\mathbf{B}_0$ and $\mathbf{v}_0$. (b) Equilibrium flow profiles $G(y)$ and their derivatives used in the present work.

The quantities F and G are the normalized equilibrium magnetic and velocity fields, respectively, in the x direction. We assume that F is given by

$$F(y)=\tanh(y) \tag{8}$$

and present results for each of the following velocity profiles,

$$G(y)=V\tanh(Ry) \tag{9a}$$

or

$$G(y)=V[1-\mathrm{sech}(Ry)], \tag{9b}$$

where V is the velocity parameter in units of the Alfvén velocity V_a. Hereafter we refer to Eq. (9a) as the tanh velocity profile and to Eq. (9b) as the sech velocity profile. The geometry of the tearing mode in Cartesian coordinates and the equilibrium quantities are shown in Fig. 1. In Fig. 1(a), the tanh velocity profile is shown, thus v_0 and B_0 have the same dependence on y (although their scales may differ). The two flow profiles and their derivatives (i.e., flow shear) are shown in Fig. 1(b). It is evident that the tanh flow profile has the largest shear at $y=0$ (the tearing layer), and the sech flow has the largest shear away from the tearing layer.

Resistive reconnection of the B_y component of the magnetic field across the tearing layer is measured by the change in the magnetic flux across $y=0$:

$$\Delta\hat{\Phi}(t)\equiv\int_0^{x_{\max}}\left|\frac{\partial}{\partial x'}\psi(x',0,t)\right|dx', \tag{10}$$

where $x_{\max}$ is one period for the periodic boundary conditions. The nonlinear growth rate $p(t)$ is given by

$$p(t)=\frac{1}{\Delta\hat{\Phi}(t)}\frac{\partial}{\partial t}\Delta\hat{\Phi}(t). \tag{11}$$

The growth rate calculated from Eq. (11) agrees with that for linear tearing (when the instability is in the linear regime) for both $V=0$ and $V\neq 0$.[11,16] Additional relevant quantities are the changes of the magnetic and kinetic energies relative to the equilibrium values, i.e.,

$$\Delta E_M(t)=\int_{y_{\min}}^{y_{\max}}\int_0^{x_{\max}}\left[\left(F+\frac{\partial\psi}{\partial y}\right)^2+\left(\frac{\partial\psi}{\partial x}\right)^2-F^2\right]dx\,dy, \tag{12a}$$

$$\Delta E_K(t)=\int_{y_{\min}}^{y_{\max}}\int_0^{x_{\max}}\left[\left(G+\frac{\partial\psi}{\partial y}\right)^2+\left(\frac{\partial\phi}{\partial x}\right)^2-G^2\right]dx\,dy. \tag{12b}$$

The total magnetic and kinetic energy

$$E_{\mathrm{tot}}(t)=\Delta E_M(t)+\Delta E_K(t)+E_{M0}+E_{K0}, \tag{12c}$$

where E_{M0} and E_{K0} are the initial magnetic and kinetic energies stored in the equilibrium shear flow and magnetic field. Because of resistive and viscous dissipation E_{tot} satisfies

$$\frac{dE_{\mathrm{tot}}}{dt}=2\int_{y_{\min}}^{y_{\max}}\int_0^{x_{\max}}\left(-\frac{J}{S}(J-F')-\frac{1}{S_v}\omega(\omega-G')\right), \tag{13a}$$

where $J=-\nabla^2\psi$ is the nonequilibrium current in the z direction, and $\omega=-\nabla^2\phi$ is the nonequilibrium vorticity. The resistive dissipation of the magnetic helicity as given by

$$\frac{d}{dt}\int_{y_{\min}}^{y_{\max}}\int_0^{x_{\max}}\psi\,dx\,dy=-\frac{1}{S}\int_{y_{\min}}^{y_{\max}}\int_0^{x_{\max}}J\,dx\,dy \tag{13b}$$

is also of interest. Equations (13a) and (13b) are valid for periodic x and zero y boundary conditions and are used as a means of estimating the quality of the numerical solutions by comparing the calculated values of the rhs and the lhs of the equations. Equation (13a) is also used to estimate the effective viscous dissipation that arises in the numerical solution of the MHD equations.

III. METHOD OF SOLUTION

We initiate the nonlinear computations with the solutions of the linearized version of Eqs. (6) and (7).[11] The amplitude factors of the linearized growing solutions are chosen so that the nonlinear terms as calculated from the linear ϕ and ψ become comparable in magnitude to the linear terms. This procedure insures that the nonlinear code is initiated at an amplitude where the subsequent evolution of the mode is in the nonlinear regime.[16] In this study the normalized spatial wave number $\alpha=2\pi/\lambda$ was 0.5, which implies that the size of the longest wavelength λ in the x direction is 4π in units of a_b. An alternating-direction implicit (ADI) finite-difference technique was used to obtain the nonlinear evolution. The solutions are first advanced one half time step in the x direction using the initial linear solutions. Next, the solutions are advanced another half time step in the y direction using the finite difference results in the x direction from the previous half time step. This procedure for a single time step is repeated until the full temporal evolution is obtained. In the x direction the finite difference form of Eqs. (6) and (7) is given by the following:

$$\frac{2}{\Delta t}\psi_{i,j}^{n+1/2}+G_j\delta_x\psi_{i,j}^{n+1/2}-F_j\delta_x\phi_{i,j}^{n+1/2}+\delta_x\psi_{i,j}^{n+1/2}\delta_y\phi_{i,j}^{n}-\delta_y\psi_{i,j}^{n}\delta_x\phi_{i,j}^{n+1/2}=\frac{2}{\Delta t}\psi_{i,j}^{n}-\frac{1}{S}J_{i,j}, \tag{14a}$$

$$\frac{2}{\Delta t}\omega_{i,j}^{n+1/2}+(\delta_y\phi_{i,j}^{n}+G_j)\delta_x\omega_{i,j}^{n+1/2}+(G_j''-\delta_y\omega_{i,j}^{n})\delta_x\phi_{i,j}^{n+1/2}+(\delta_y\psi_{i,j}^{n}+F_j)\delta_x J_{i,j}^{n+1/2}-(F_j''-\delta_y J_{i,j}^{n})\delta_x\psi_{i,j}^{n+1/2}=\frac{2}{\Delta t}\omega_{i,j}^{n}+\frac{1}{S_v}(\delta_x^2+\delta_y^2)\omega_{i,j}^{n}, \tag{14b}$$

where $\Delta t=t_{n+1}-t_n$, and

$$J^n_{i,j}=-(\delta_x^2+\delta_y^2)\psi^n_{i,j}, \quad \omega^n_{i,j}=-(\delta_x^2+\delta_y^2)\phi^n_{i,j}$$

The grid spacing in the x direction is uniform, thus the finite differences are given by

$$\delta_x\psi^n_{i,j}=\frac{\psi^n_{i+1,j}-\psi^n_{i-1,j}}{2\Delta x}, \quad \delta_x^2\psi^n_{i,j}=\frac{\psi^n_{i+1,j}-2\psi^n_{i,j}+\psi^n_{i-1,j}}{(\Delta x)^2},$$

where $\Delta x=\frac{1}{2}(x_{i+1}-x_{i-1})$, while in the y direction

$$\delta_y\psi^n_{i,j}=\frac{1}{2}\left(\frac{\psi^n_{i,j+1}-\psi^n_{i,j}}{y_{j+1}-y_j}+\frac{\psi^n_{i,j}-\psi^n_{i,j-1}}{y_j-y_{j-1}}\right),$$

$$\delta_y^2\psi^n_{i,j}=\frac{2}{y_{j+1}-y_{j-1}}\left(\frac{\psi^n_{i,j+1}-\psi^n_{i,j}}{y_{j+1}-y_j}-\frac{\psi^n_{i,j}-\psi^n_{i,j-1}}{y_j-y_{j-1}}\right).$$

The variable grid spacing $\Delta y_j=y_{j+1}-y_j$ expands from a minimum of $\Delta y_{\min}=10^{-3}$ at the tearing layer to $\Delta y_{\max}=0.5$ near the computational boundaries according to the prescription

$$\Delta y_j=\Delta y_{\max}(\Delta y_{\min}/\Delta y_{\max})^{(j_{\max}-j)/(j_{\max}-1)},$$

where $j_{\max}$ denotes the boundary grid point. Up to 200 grid points in the y direction and up to 64 grid points in the x direction were used. Constant grid spacing in the y direction was also used for low S values. Fourth-order smoothing[23] was applied to the solutions away from the tearing layer. Equations (14a) and (14b) are written in tridiagonal form

$$-A^n_i U^{n+1/2}_{i+1,j}+B^n_i U^{n+1/2}_{i,j}-C^n_i U^{n+1/2}_{i-1,j}=D^n_{i,j}, \tag{15}$$

where A, B, and C are 2×2 matrices, and U and D are two-dimensional vectors. Equation (15) is solved for U using Gaussian elimination. For the next half time step $n\rightarrow n+\frac{1}{2}$ and $n+\frac{1}{2}\rightarrow n+1$ in the above Eq. (15), and the solutions are advanced one time step. The boundary conditions are $\psi(y=\pm y_{\max})=0$ and $\phi(y=\pm y_{\max})=0$, where $y_{\max}$ is the distance to the boundary from the tearing layer, and both ψ and ϕ are periodic in the x direction. Because of the presence of the symmetry breaking equilibrium shear flow, one cannot use the simplifying symmetry assumptions that enable the solutions of the MHD equations to be computed in one-quarter of the present domain.[16] Also, the imposing of the periodic boundary conditions requires one to pass through the mesh three times for each integration in the x direction.[14] Only two passes through the mesh are necessary in the nonperiodic y direction.

For a fully implicit scheme the time step Δt is limited by $\Delta t<\Delta x/V_{\max}$, where $V_{\max}$ is the maximal Alfvén velocity anywhere on the grid.[24] In our case the terms

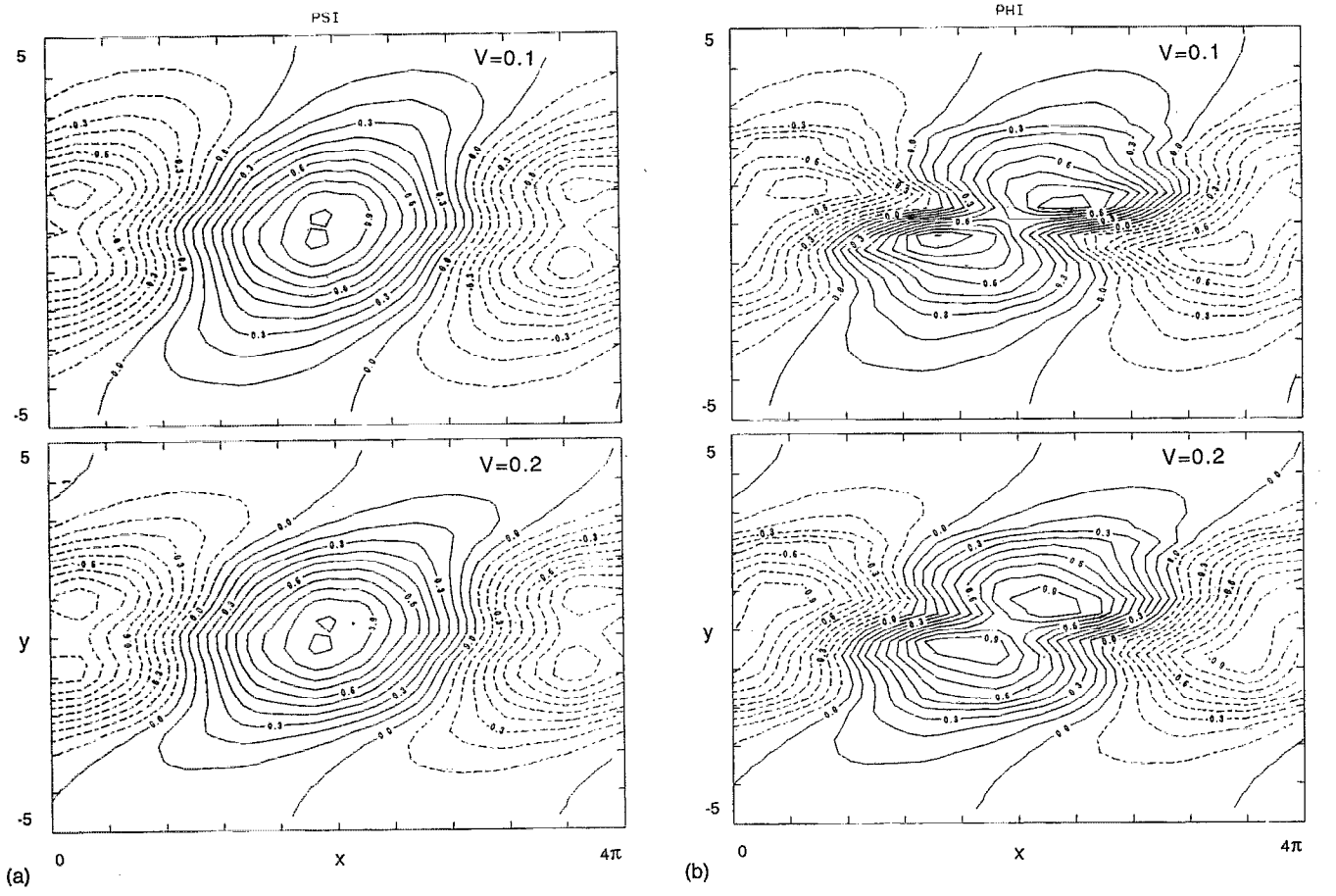

FIG. 2. Spatial dependence of the flux function and streamfunction with $S=10^2$, and tanh equilibrium flow profile. (a) The flux function ψ with $V=0.1$ (top figure) and $V=0.2$ (bottom figure). (b) The streamfunction ϕ with $V=0.1$ (top figure) and $V=0.2$ (bottom figure).

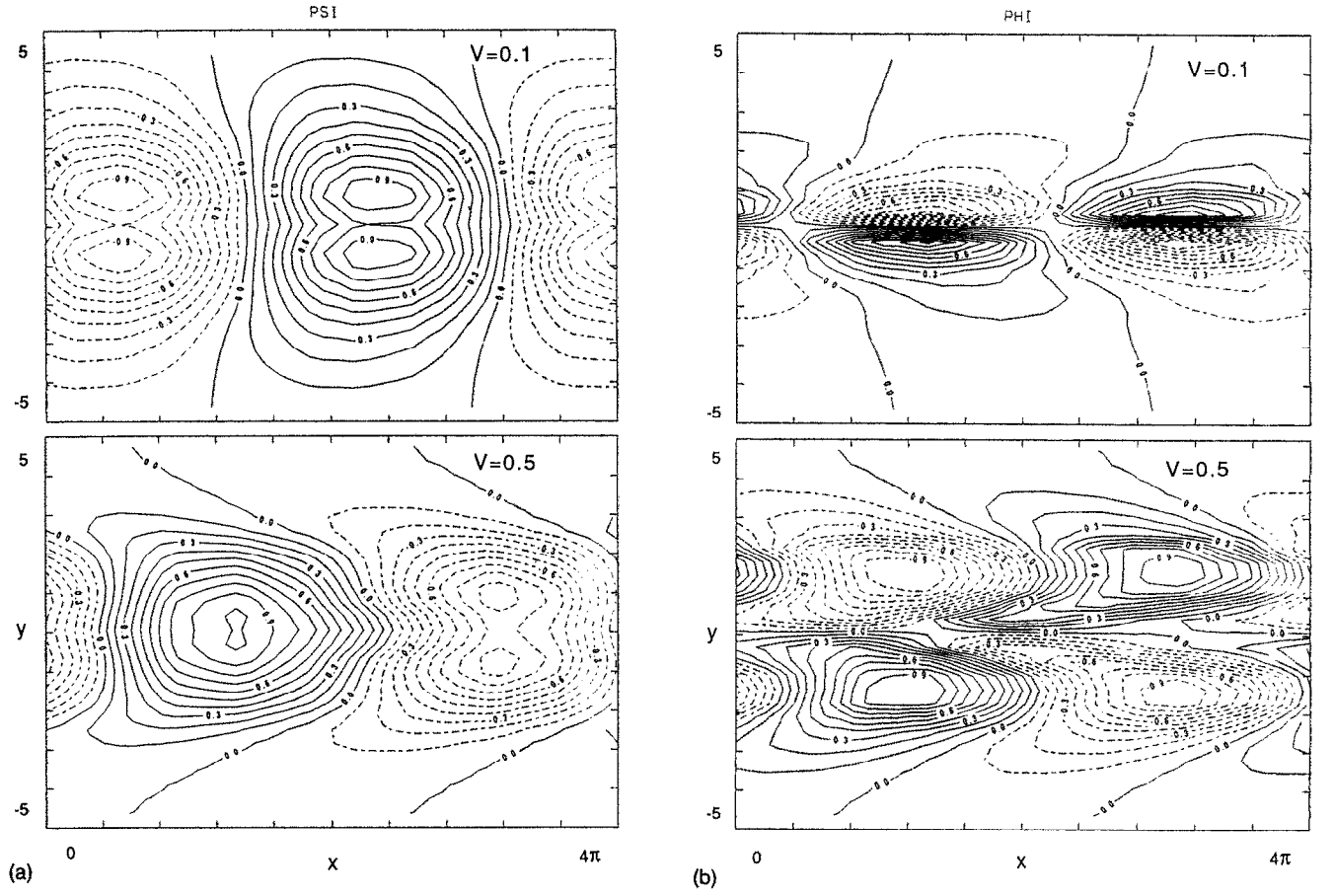

FIG. 3. Spatial dependence of the flux function and streamfunction with $S=10^2$, and sech equilibrium flow profile. (a) The flux function ψ with $V=0.1$ (top figure) and $V=0.5$ (bottom figure). (b) The streamfunction ϕ with $V=0.1$ (top figure) and $V=0.5$ (bottom figure).

higher than second order are treated explicitly, and it has been found that the relation $\Delta t<\Delta x/2$ gives satisfactory results. When nonconstant grid spacing is used, Δx is one or several orders of magnitude larger than Δy across the tearing layer. Reasonable computation times on a Cray II for S as large as 10^6 are possible with this technique. A typical run with $S=10^4$ takes about 30 min of CPU time.

IV. NUMERICAL RESULTS

We initiate the nonlinear evolution with a single linear mode in the x direction. The size of the computational domain in the x direction is determined by the normalized wavelength $\alpha=k_x a_b$ of the linear mode. We use $\alpha=0.5(x_{\max}=2\pi/\alpha=4\pi)$ to initiate the calculations. The phase shift between ψ and ϕ in the linear stage is caused by the equilibrium shear flow. Detailed treatments of the linear tearing mode with flow are given in Einaudi and Rubini[9,10] and Ofman *et al.*[11]

In Figs. 2–12 we examine the spatial structure and the temporal evolution of the nonlinear tearing mode with flow. In these runs the parameters were $S=10^2$, 10^4, 10^5, $R=0.73$, $\alpha=0.5$, and the flow parameter was $V=0$, 0.1, 0.2, 0.3, 0.5 for the tanh flow profile, while $V=0.1$, 0.5 for the sech flow profile.

The spatial variations of ψ, ϕ, Ψ, and Φ, and the current $J_T=J-F'$ after two resistive times, normalized to their respective maximal values, are shown in Figs. 2–6. In Fig. 2 the equilibrium shear flow is the tanh velocity profile, with $V=0.1$ and $V=0.2$. In Fig. 3 the equilibrium shear flow is the sech velocity profile with $V=0.1$ and $V=0.5$. The other parameters for both cases are $S=10^2$, $R=0.73$, and $\alpha=0.5$. When $V=0$, ψ is symmetric with respect to the x and y axes, while ϕ is antisymmetric in both the linear and nonlinear regimes. When flow is present, this symmetry is broken and the perturbations align themselves with the equilibrium flow. Namely, in Fig. 2, ψ and ϕ deform in opposite directions with respect to the x axis, and the distortion away from the tearing layer increases with V. Similar alignment with the flow occurs for sech equilibrium in Fig. 3, but for larger V the values of ψ and ϕ are distorted more near the tearing layer (where the shear is zero) than away from it, in agreement with the stabilizing effect of higher shear regions [see Fig. 1(b)] as expected from the linear theory.[7,8]

The contour lines of the total flux function and streamfunction for the tanh flow profile at $t=200\tau_h$, with $V=0.5$ and $S=100$, are shown in Fig. 4. The velocity and the magnetic field lines are parallel to the contours of Ψ and Φ. The magnetic field lines exhibit the saturated island struc-

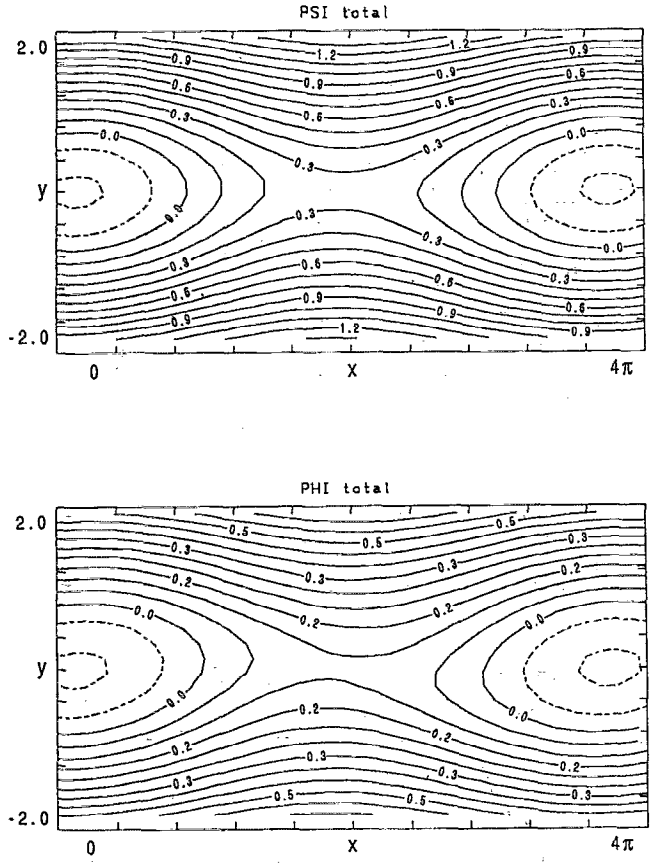

FIG. 4. The total flux function Ψ and the total streamfunction Φ with $V=0.5$, $S=10^2$, and the tanh flow profile.

ture, where the island width is an order of magnitude larger than the linear tearing layer scale length[7]

$$\epsilon=[\alpha F'(0)S]^{-1/3}. \tag{16}$$

Similar island structures appear in the contour plot of Φ. The appearance of the streamfunction is different from the standard case[1] due to the presence of the equilibrium shear flow. Namely, instead of the four contra-rotating flow vortices, an island (similar to the magnetic island) is formed in the flow pattern of the plasma. Note that the x point in the center of the contour plot of Φ is distorted in agreement with the structure of ϕ in Fig. 2(b) and small distortion of the magnetic x point appears in the contour plot of Ψ.

We present the low-resistivity solutions with $S=10^4$, $V=0.1$, and the sech flow profile at $t=2000\tau_h$ in Fig. 5. In Fig. 5(a) contours of Ψ and Φ are shown, while in Fig. 5(b) the contours of ψ and ϕ are displayed. The saturated magnetic island structure is evident in the contours of Ψ. The width of the islands is an order of magnitude larger than the linear tearing layer scale length ϵ with similar parameters. For $S=10^4$ both the tearing layer width and the island width are smaller than for $S=10^2$ as expected from the linear ϵ scaling with resistivity. The appearance of sharp features along the y axis indicates the narrow tearing layer. It is interesting to compare the contours of ψ in Fig. 5(b) to the contours of ψ in Fig. 3(a). In both figures similar sharp features form along the y axis, indicating that the tearing layer is narrow compared to the high-resistivity, low-shear-flow cases. In Fig. 5(b) this is due to the low resistivity ($S=10^4$ with $V=0.1$), while in Fig. 3(a) this is due to the high shear flow ($V=0.5$ with $S=10^2$). For the sech profile the flow near the y axis is small compared to the flow away from the y axis, and thus the contour of Φ shows a relatively flat region of width a_b along the y axis, where ϕ and its vortices are dominant. The effect of the narrow boundary layer is clearly seen in Fig. 5(b).

The dependence of the saturated magnetic island width W on the tanh and sech shear flow profiles is shown in Fig. 6. The top two curves are for $S=10^2$, and the bottom two curves are for $S=10^3$. When $V=0$ the saturated magnetic island width $W=3.3a_b$. When the flow is tanh and $S=10^2$, $V=0.5$, the width of the magnetic islands decreases by 50% with respect to the $V=0$ case. The effect of the sech flow is smaller for the same S and V, and W decreases by 25%. When $S=10^3$ the $V=0$ saturated island width is $2.4a_b$. When small shear flow is present W decreases rapidly, while larger flow $V>0.3$ does not affect the island width considerably. This is consistent with the transition from the $S^{-2/5}$ linear growth rate scaling for the $V=0$ tearing mode[1] to the $S^{-1/2}$ linear growth rate scaling when the shear flow is comparable to the magnetic shear.[7] The tanh flow shear profile $G'(y)$ peaks at the resonant surface, while for sech flow profile $G'(y)$ has extrema outside the resonant surface, hence, the island growth is reduced more effectively by the tanh flow profile [see Fig. 1(b)].

The current J_T for $V=0$ and $V=0.3$ (tanh velocity profile) is shown in Fig. 7. When $V=0$ the current is symmetric with respect to the x and y axes and its maximum $J_{T\max}$ occurs near the center of the slab and points in the negative z direction. When $V=0.3$ the current has a more complicated two-dimensional structure, again aligned with the equilibrium flow. Additional regions of significant current appear far from the tearing layer, around $y=\pm 2.5$ with $|J_T(x,2.5)/J_{T\max}| \sim 0.2$, thus the flow generates significant currents in the external regions of the tearing mode.

Figure 8 depicts the temporal evolution of the growth rate, the reconnected flux, and the perturbed magnetic, kinetic, and total energies for eight resistive times ($800\tau_h$) with $V=0.1$, the tanh flow profile, and $S=10^2$. In Fig. 8(a) we present the temporal evolution of the growth rate (curve A) and the reconnected flux (curve B). Initially the growth rate calculated from Eq. (11) corresponds to the linear growth calculated directly from the exponential growth of the solutions,[11] and the reconnected flux grows exponentially with time. After $10\tau_h$ the growth rate drops considerably and the reconnected flux grows linearly with time as expected in the Rutherford regime.[13] After another $100\tau_h$ the growth of the reconnected flux slows to less than the linear rate. After $400\tau_h$ the mode saturates completely, and the amount of the reconnected flux remains practically constant with time. The growth rate continues to decrease at an exponential rate.

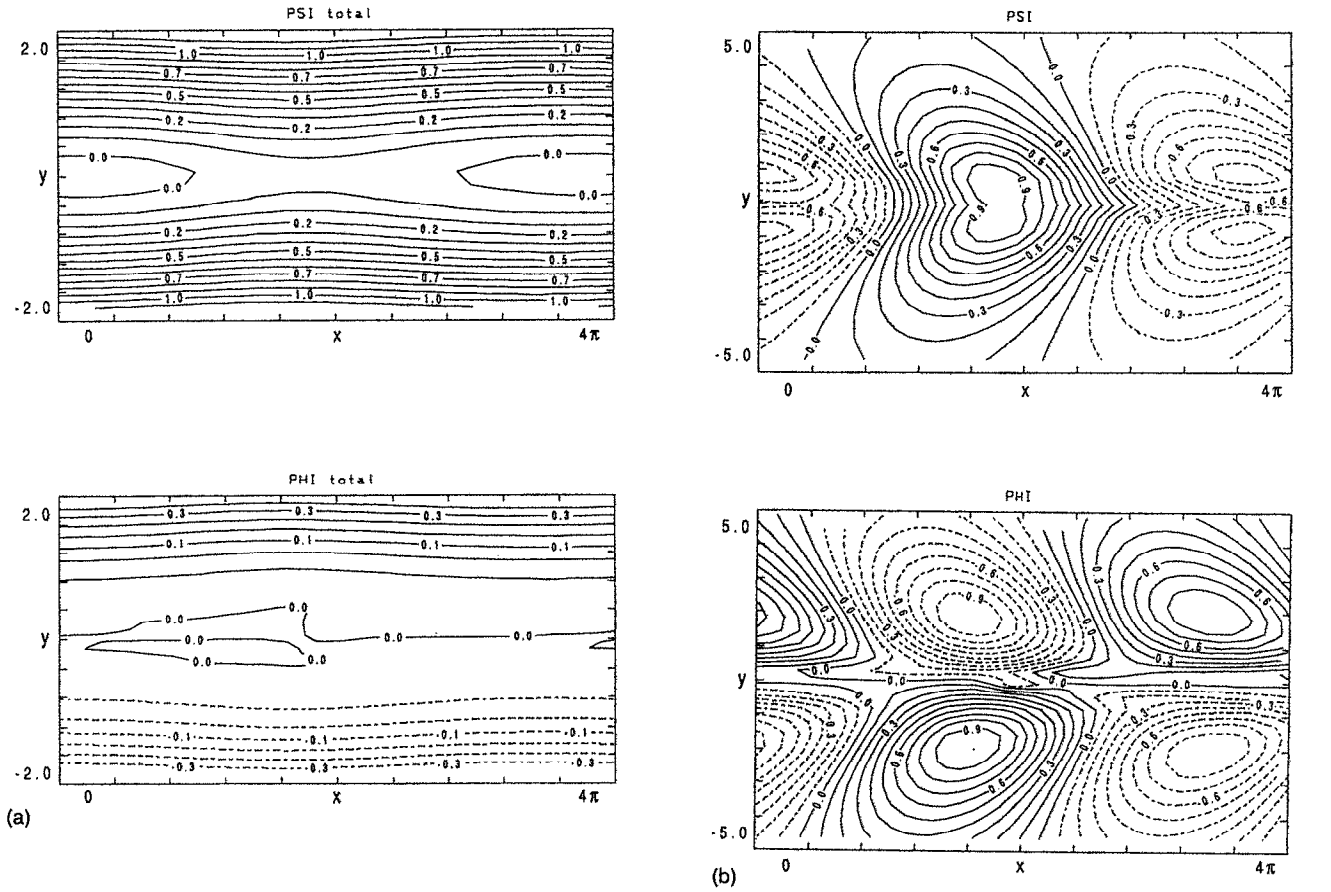

FIG. 5. Contours of the flux function and the streamfunction with $V=0.1$, $S=10^4$, and the sech flow profile: (a) Ψ and Φ, (b) ψ and ϕ.

In Fig. 8(b) curve A represents the change of the magnetic energy in the x component of the magnetic field ΔE_{Mx} [defined by setting $\partial\psi/\partial x=0$ in Eq. (12a)], while curve B represents the change of the magnetic energy in the y component, ΔE_{My} (defined by $\Delta E_M=\Delta E_{Mx}+\Delta E_{My}$).

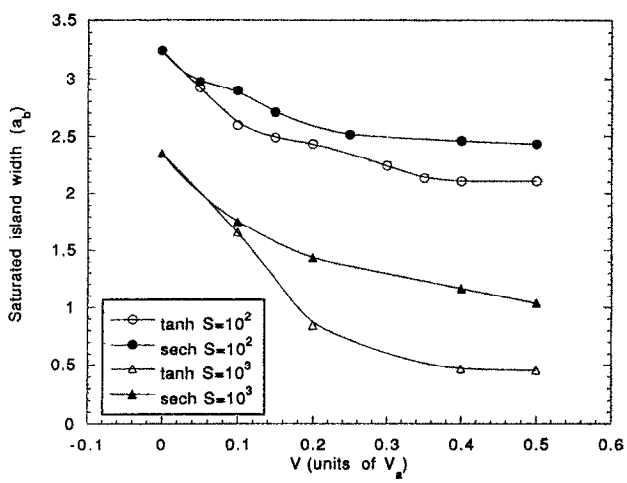

FIG. 6. The dependence of the saturated island width on V for $S=10^2$ with sech flow profile (full circles) and tanh flow profile (empty circles), and for $S=10^3$ with sech flow profile (full triangles) and tanh flow profile (empty triangles).

Curve C corresponds to the total change of the magnetic and kinetic energies $\Delta E_{\rm tot}\equiv\Delta E_m+\Delta E_k$. All these quantities are presented on a log scale, thus their absolute values are shown—ΔE_{Mx} and $\Delta E_{\rm tot}$ are negative for most of the evolution time indicating energy loss. The changes of sign of $\Delta E_{\rm tot}$ and ΔE_{Mx} appear as sharp minima at $t\approx 5$ and $t\approx 30$, respectively. Most of the transfer of energy occurs from the x component of the magnetic field to the y component (curve B) and to resistive dissipation. A small fraction of ΔE_{My} is transferred to the kinetic energies (see Table I). The change of the kinetic energies ΔE_K in Fig. 8(c) is initially comparable in magnitude (but opposite in sign) to ΔE_M, but after about one resistive time ΔE_{Kx} saturates at values an order of magnitude smaller than ΔE_M, and the transition from exponential to linear growth occurs in a time $t<100\tau_h$, when ΔE_{Ky} is an order of magnitude smaller than ΔE_{Kx}.

In Fig. 9 we compare the change in the magnetic and total energies for the cases $V=0.2$ and $V=0.3$ with $S=10^2$. For $V=0.3$ the rate of change of the energies is initially ($t<100\tau_h$) lower than for $V=0.2$, but after the growth saturates the changes occur at similar rates. The initial wiggling of the total energy is due to transient effects that arise when the nonlinear code is initiated with the linear solutions. The total energy release of the tearing mode with $V=0.3$ is only 60% of the energy released when

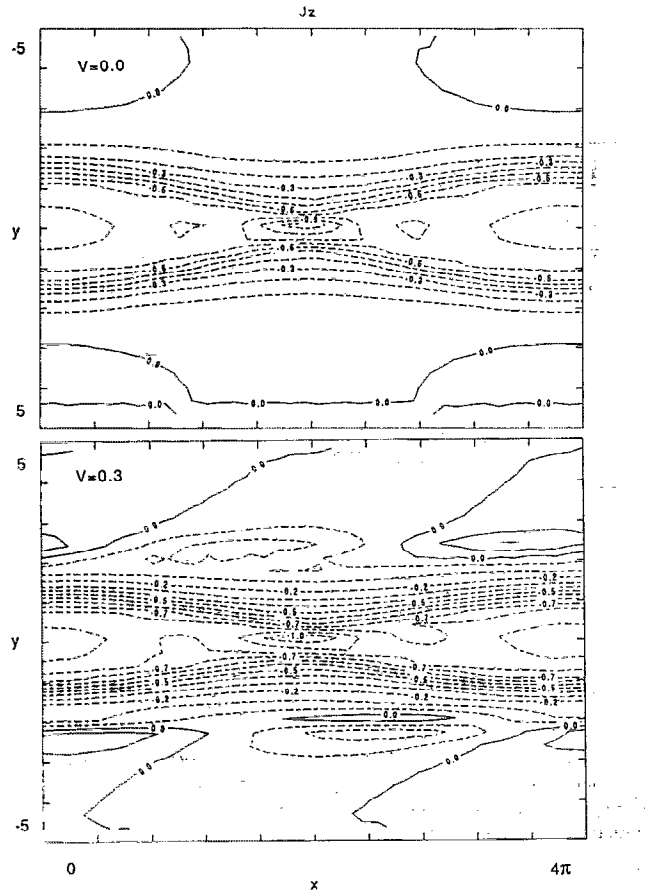

FIG. 7. Contours of the current $J=-\nabla^2\psi$ with $V=0.0$ (top figure) and $V=0.3$ (bottom figure), and the tanh flow profile with $S=10^2$.

$V=0.2$. This decrease of energy release with increasing V is a trend seen in all runs as evidenced in Table I.

The case where $S=10^4$, $V=0.5$, with the tanh equilibrium flow profile is presented in Fig. 9 up to a time $2000\tau_h$. The temporal behavior of the $S=10^4$ case is similar to the $S=10^2$ case but, as expected from the lower resistivity, proceeds on a longer time scale. The absolute values of the magnetic and total energy changes are shown in Fig. 10(a). Note that the change of sign of $E_{\rm tot}$ (curve C) occurs at $\sim 700\tau_h$ that is about an order of magnitude smaller than for $S=10^2$. This is consistent with the linear growth rate scaling of $S^{-1/2}$ for the tearing mode with flow. In Fig. 10(b) total energy dissipation (curve A) is compared to the resistive dissipation (curve B). Due to an initial transient instability, the total energy dissipation exhibits rapid oscillations that decay within several hundred Alfvén times, and the evolution proceeds with the resistive dissipation being significantly larger than the dissipation due to numerical viscosity. This is verified by comparing the calculated resistive dissipation term to the total energy dissipation term in Eq. (13a). The quantities ΔE_{Kx} and ΔE_{Ky} are shown in Fig. 10(c). The initial exponential growth slows down after only $500\tau_h$, and the nonlinear effects are evident. The change in the kinetic energies after $1000\tau_h$ is an order of magnitude lower than the change in the magnetic energies in Fig. 10(a), thus the energy release is dominated by resistive effects. Nonlinear saturation of the growth rate (curve A) and the reconnected flux (curve B) are presented in Fig. 10(d). The growth rate defined in Eq. (11) decreases by a factor of 2 after $2000\tau_h$ and the slower than exponential growth of the reconnected flux is evident after $500\tau_h$. This is consistent with the tendency toward nonlinear saturation of the energies in Figs. 10(a) and 10(b).

In Fig. 11 we present the temporal evolution of the energies for $S=10^5$, $V=0.5$, and the tanh flow profile. The initial ΔE_{Mx} is 1.5 times larger than ΔE_{Mx} in the case where $S=10^4$, and it becomes negative after $\sim 1700\tau_h$. Its slower evolution is consistent with the $S^{-1/2}$ linear growth rate scaling, and, due to the large resistive time, the nonlinear effects are still not significant after $2000\tau_h$ or $0.02\tau_r$. The kinetic energies in Fig. 11(b) evolve with the corresponding linear growth rate. From the previous results for $S=10^2$ and $S=10^4$, it is evident that the nonlinear saturation becomes significant on a time scale of $0.1\tau_r$ that corresponds to $10^4\tau_h$ for $S=10^5$.

The distribution of energies at saturation for several values of V with the tanh and sech equilibrium flow are presented in Fig. 12 and at $t=200\tau_h$ ($S=10^2$) and $t=2000\tau_h$ ($S=10^4$) in Table I. The calculated distribution of energies for the cases with $V=0$ agrees with the results obtained by Steinolfson and Van Hoven.[16] The dependence of the energies on V with $S=10^2$ at $t=500\tau_h$ is shown in Fig. 12. When $S=10^2$ (as noted above) the change in the magnetic energy decreases with V [Fig. 12(a)], while the change in the kinetic energy increases with V [Fig. 12(b)]. When $V=0.3$ and the tanh flow profile, the release of the magnetic energy ΔE_{Mx} and the change in total energy $\Delta E_{\rm tot}$ are more than three times lower than that for $V=0$. At the same time, ΔE_{Kx} increased by about one order of magnitude and ΔE_{Ky} increased by a factor of ~ 35. When V is varied in the presence of the sech equilibrium flow profile, the absolute values of ΔE_{Mx}, ΔE_{My}, and $\Delta E_{\rm tot}$ vary at a slower rate than in the presence of the tanh equilibrium flow profile. When $V>0.3$ the decrease of energy release slows down and does not change significantly up to $V=0.5$. This is consistent with the larger saturated magnetic island width obtained with the sech flow profile than with the tanh flow profile for the same parameter values and the leveling off of the saturated island width for $V>0.3$ (see Fig. 6).

When $S=10^4$ (see Table I) and $V=0.5$ the release of the magnetic energy at $t=2000\tau_h$ is 25% of ΔE_{Mx} when $V=0.1$ and less than one-fifth of energy released without equilibrium flow. When $V=0.5$ the change in the kinetic energies is an order of magnitude smaller than the change in the magnetic energy, and, when $V=0.1$, ΔE_K is two orders of magnitude smaller than ΔE_M. The kinetic energy is even less significant when $V=0$.

Figure 13 is devoted to the calculation of the conservation relations of Eqs. (13a) and (13b). As a test of the overall behavior of the numerical code we calculated the temporal change in the total energy, and the magnetic helicity for $V=0.3$ with the tanh profile, and compared it to

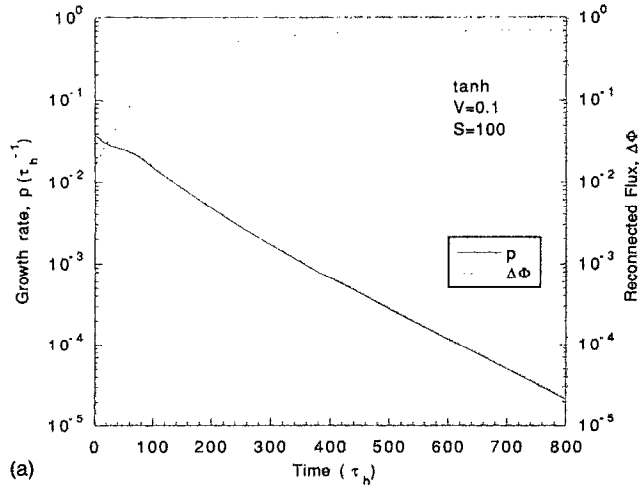

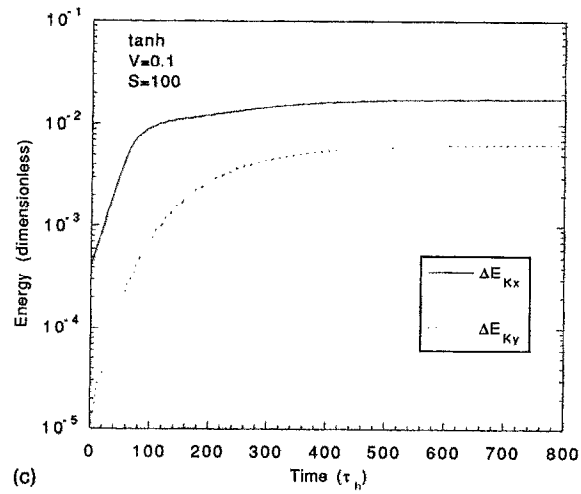

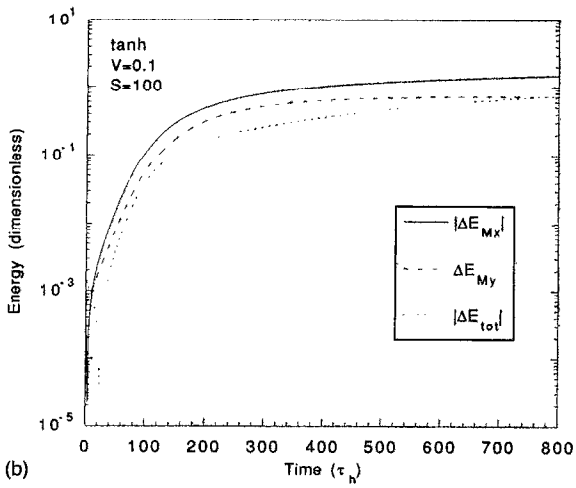

FIG. 8. The temporal evolution for the case where $S=10^2$, and $V=0.1$ with the tanh equilibrium flow profile. (a) The growth rate p and the reconnected flux $\Delta\hat{\Phi}$. (b) The change in the x component and in the y component of the magnetic energy ΔE_M. The change in the total energy $\Delta E_{\rm tot}$. (c) The change in the x component, and in the y component of the kinetic energy ΔE_K.

the resistive dissipation according to Eqs. (13a) and (13b). After an initial transit period of $\sim 20\tau_h$ a very good agreement is seen between the calculated energy dissipation and the resistive dissipation. The initial ($\lesssim 30\tau_h$) energy discrepancy is due to transient numerical solutions excited initially in the nonlinear code. The value of the actual viscosity in the code was estimated using the energy conservation relation [Eqs. (13a) and (13b)] and was found to be $S_v=1.2\times 10^3$ for this case. The calculated values of S_v were found to depend strongly on the amount of the numerical fourth-order smoothing applied to the solutions, and were in the range 10^3–10^5. In the case of helicity

TABLE I. The change in the magnetic, kinetic, and total energies.

V	ΔE_{Mx}	ΔE_{My}	ΔE_{Kx}	ΔE_{Ky}	$\Delta E_{\rm tot}$
		$S=10^2$, $t=200\tau_h$			
0.0	-0.792	0.488	0.94×10^{-2}	0.73×10^{-3}	-0.294
tanh flow profile					
0.1	-0.482	0.305	1.24×10^{-2}	2.71×10^{-3}	-0.162
0.2	-0.296	0.189	1.76×10^{-2}	5.71×10^{-3}	-8.37×10^{-2}
0.3	-0.237	0.153	2.58×10^{-2}	9.86×10^{-3}	-4.83×10^{-2}
		$S=10^4$, $t=2000\tau_h$			
0.0	-9.11×10^{-2}	4.38×10^{-2}	1.44×10^{-5}	4.74×10^{-7}	-4.73×10^{-2}
tanh flow profile					
0.1	-4.38×10^{-2}	1.85×10^{-2}	6.90×10^{-4}	1.41×10^{-4}	-2.45×10^{-2}
0.5	-1.27×10^{-2}	4.89×10^{-3}	1.48×10^{-3}	8.94×10^{-4}	-5.54×10^{-3}
sech flow profile					
0.1	-6.35×10^{-2}	2.84×10^{-2}	9.28×10^{-5}	4.30×10^{-5}	-3.49×10^{-2}
0.5	-1.58×10^{-2}	7.38×10^{-3}	6.13×10^{-4}	1.32×10^{-4}	-7.65×10^{-3}

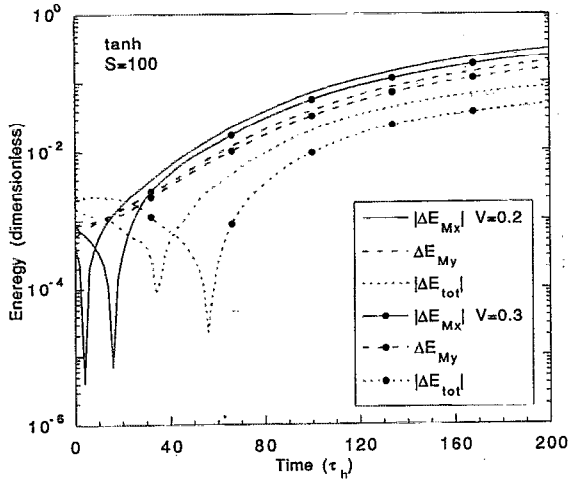

FIG. 9. As in Fig. 8(b), but with $V=0.2$ and $V=0.3$.

the conservation was two orders of magnitude better than the resistive energy dissipation.

V. SUMMARY

We have extended the nonlinear tearing studies of Steinolfson and Van Hoven[16] to include the effects of shear flow. We have also extended the studies by Persson[18,19] and Persson and Bondeson[17] using the finite-difference ADI method (which is not limited to a small number of modes as in the Persson[18,19] and Persson and Bondeson[17] studies) to solve the 2-D incompressible resistive MHD equations in slab geometry. We have studied the effect of both symmetric and antisymmetric shear flow profiles on the magnetic and kinetic energies, and on the saturated magnetic island width of the tearing mode in the lower resistivity range. In the parameter range of our studies the tearing mode was found to saturate monotonically to a quasi-steady-state rather than an oscillatory state as found by Persson[18,19] and Persson and Bondeson.[17] The saturated island width was found to decrease by 80% when shear

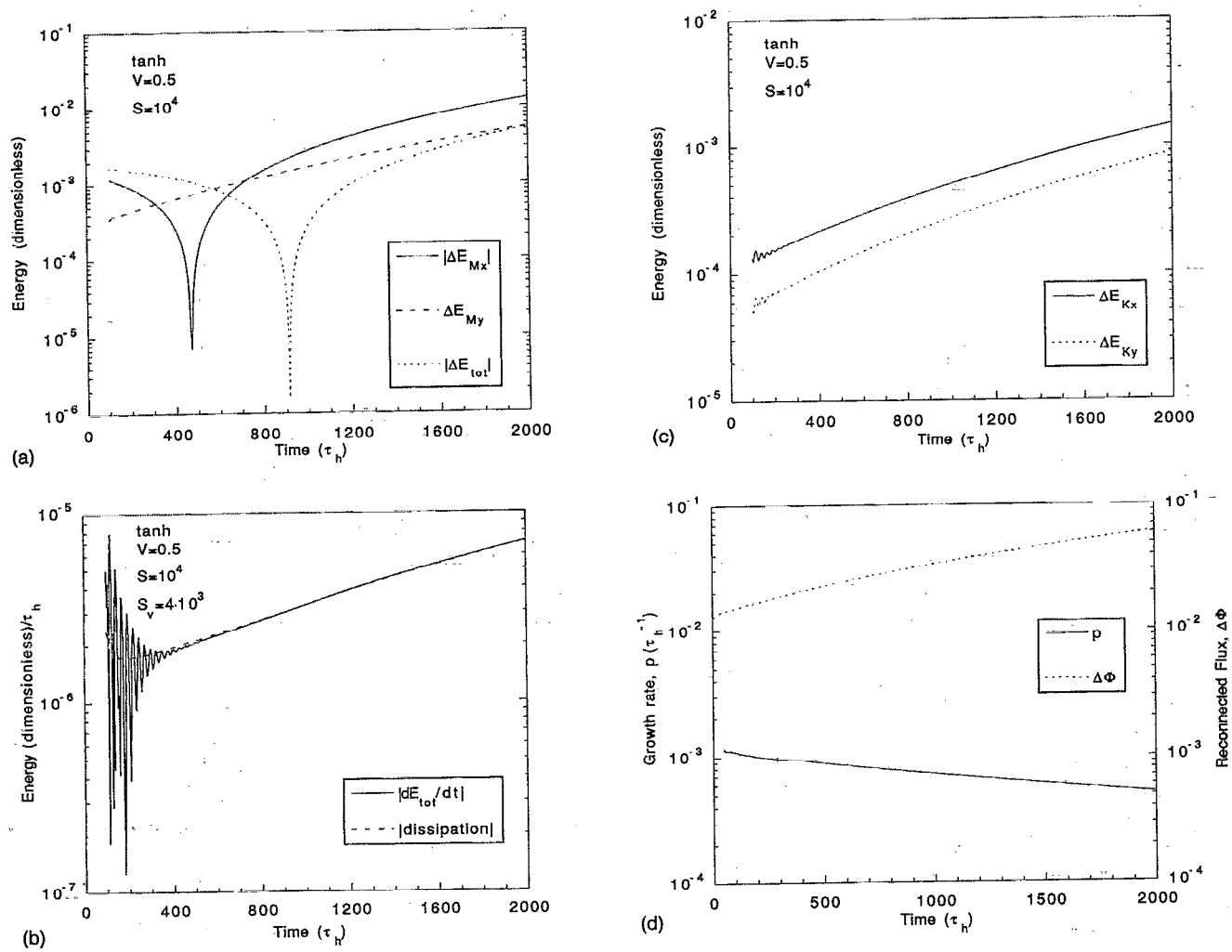

FIG. 10. The nonlinear evolution of the $S=10^4$ and $V=0.5$ tearing mode with the tanh equilibrium flow profile. (a) The change in the x component and in the y component of the magnetic energy ΔE_M. The change in the total energy ΔE_{tot}. (b) The total energy dissipation dE_{tot}/dt and the dissipation calculated from the rhs of Eq. (13a). (c) The change in the x component and in the y component of the kinetic energy ΔE_K. (d) The temporal evolution of the growth rate p and the reconnected flux $\Delta\hat{\Phi}$.

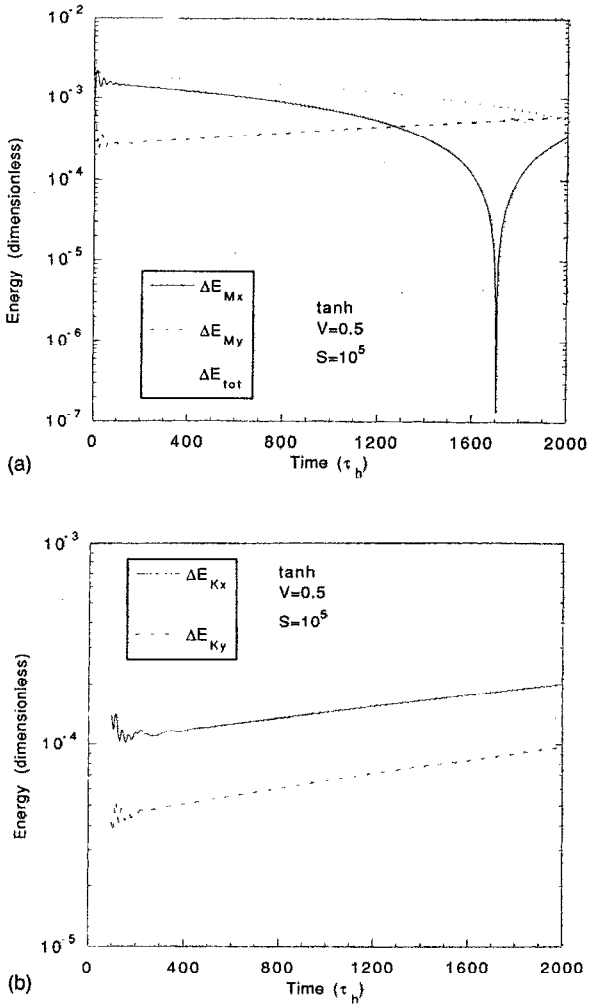

FIG. 11. The nonlinear evolution for the case where $S=10^5$ and $V=0.5$ with the tanh equilibrium flow profile: (a) ΔE_{Mx}, ΔE_{My}, $\Delta E_{\rm tot}$, (b) ΔE_{Kx}, ΔE_{Ky}.

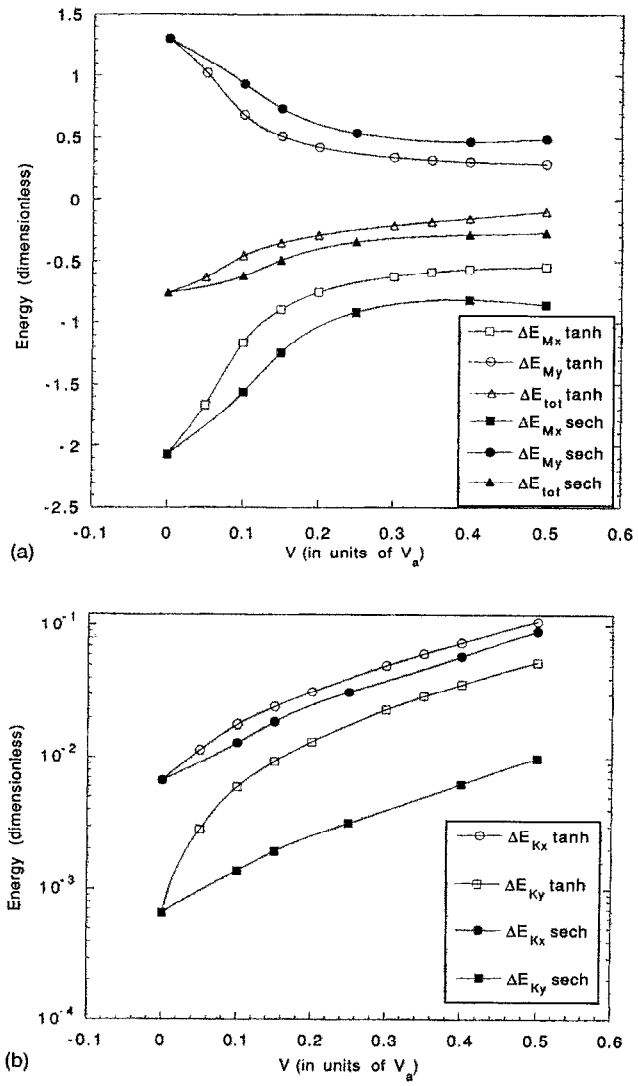

FIG. 12. The dependence of ΔE_{Mx}, ΔE_{My}, ΔE_{Kx}, ΔE_{Ky}, and $\Delta E_{\rm tot}$ at $t=500\tau_h$ with $S=10^2$ on V for the tanh and the sech flow profiles.

flow is present ($V>0.3$, $S=10^3$, and the tanh flow profile). It has been found that the suppression of the magnetic island growth due to the tanh flow profile was significantly larger (up to $\sim 50\%$ more of island width reduction) than the effect of the sech flow profile.

We have investigated the effect of equilibrium shear flow on the evolution of the nonlinear tearing mode, via numerical solution of incompressible resistive MHD equations, with V ranging up to $0.5V_a$, and $10^2 \leqslant S \leqslant 10^5$. The perturbed flow function and streamfunction lose the symmetries of the $V=0$ tearing mode and are found to distort in the direction of the equilibrium shear flow. Their mode structure in the x direction, determined initially by the linear wave number α, is not greatly affected during the nonlinear evolution. Additional currents are generated far from the tearing layer by the presence of relatively small shear flow, in agreement with the linear result that flow has a significant effect on the external region of the tearing mode. The amount of the released magnetic energy decreased with increasing V by more than 50%, for both low-resistivity ($S=10^4$) and high-resistivity ($S=10^2$) tearing. Exponential decrease of the growth rate with time occurred in all the calculated cases; its time scale was primarily determined by the resistivity and the shear flow. Empirically the growth rate can be approximated by

$$p = a p_{\rm lin} e^{-\beta t}, \quad t > t_0, \tag{17}$$

where $p_{\rm lin}$ is the linear growth rate, $t_0 \approx \tau_r$, $a=O(1)$, and $\beta=\beta(S,V,S_v)$ for a given α, R, and flow profile. Nonlinear saturation of the energies was found to become significant after $0.1\tau_r$. The change in the kinetic energy was seen to be two orders of magnitude lower than the magnetic energy release for small V, and one order of magnitude lower for large $V=0.5$. The total energy and helicity dissipation were calculated and found to agree with Eqs. (13a) and (13b).

A velocity shear layer was observed to form naturally at a boundary region of magnetically confined plasma.[25,26] One potential application of the present results is to explain the experimental observations of the improved confinement

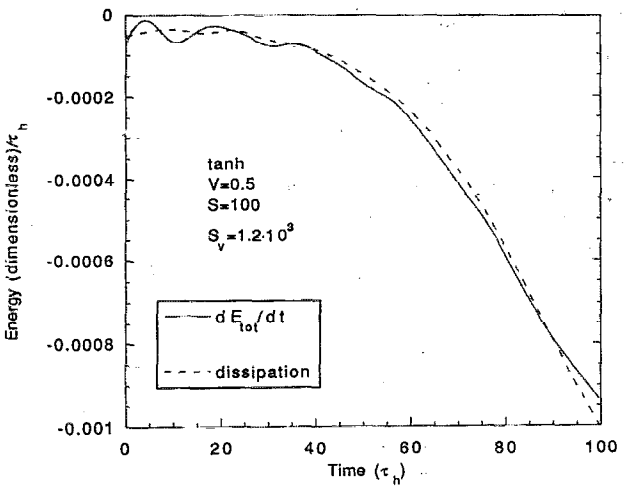

FIG. 13. The energy dissipation as calculated from the lhs of Eq. (13a) and the rhs of Eq. (13a) with $S=10^2$ and $V=0.3$.

associated with the increase of the velocity shear at the edge region of the tokamak.[27] An additional potential application is to flaring loops, a phenomenon that occurs when magnetic flux tubes rise through the sheared magnetic fields of solar active regions. The loops often have flows parallel to their axis[28] and, hence, most likely parallel to the magnetic field. It is well known that the growth of the usual tearing mode without flow and with classical dissipation is an order of magnitude too slow to explain the rapid energy release in such loops.[29] The growth rate can be increased, of course, if the dissipative effects are somehow increased by nonclassical effects, such as turbulence. However, no generally accepted theory has been developed for such enhanced dissipation. Therefore, at least for classical dissipation, the present results predict that the tearing mode is even *less* likely to play a role in the energy release in flaring loops with flows.

ACKNOWLEDGMENTS

This work was supported by U.S. Department of Energy Contract No. DE-FG05-80ET-53088 and National Science Foundation Contract No. ATM-90-15705.

[1]H. P. Furth, J. Killeen, and M. N. Rosenbluth, Phys. Fluids **6**, 459 (1963).
[2]H. Wang and H. Zirin, BAAS **22**, 2 (1990).
[3]E. R. Priest, *Solar Magnetohydrodynamics* (Reidel, Dordrecht, The Netherlands, 1985).
[4]R. B. Paris and W. N.-C. Sy, Phys. Fluids **26**, 2966 (1983).
[5]M. Dobrowolny, P. Veltri, and A. Mangeney, J. Plasma Phys. **29**, 303 (1983).
[6]F. Porcelli, Phys. Fluids **30**, 1734 (1987).
[7]X. L. Chen and P. J. Morrison, Phys. Fluids B **2**, 495 (1990).
[8]X. L. Chen and P. J. Morrison, Phys. Fluids B **2**, 2575 (1990).
[9]G. Einaudi and F. Rubini, Phys. Fluids **29**, 2563 (1986).
[10]G. Einaudi and F. Rubini, Phys. Fluids B **1**, 2224 (1989).
[11]L. Ofman, X. L. Chen, P. J. Morrison, and R. S. Steinolfson, Phys. Fluids B **3**, 1364 (1991).
[12]L. Ofman, Phys. Fluids B **4**, 2751 (1992).
[13]P. H. Rutherford, Phys. Fluids **16**, 1903 (1973).
[14]D. D. Schnack, Ph.D. thesis, University of California, Davis, 1977.
[15]D. D. Schnack and J. Killeen, Nucl. Fusion **19**, 877 (1979).
[16]R. S. Steinolfson and G. Van Hoven, Phys. Fluids **27**, 1207 (1984).
[17]M. Persson and A. Bondeson, Phys. Fluids B **2**, 2315 (1990).
[18]M. Persson, Ph.D. thesis, Chalmers University of Technology, Göteborg, 1987.
[19]M. Persson, Nucl. Fusion **31**, 382 (1991).
[20]X. L. Chen and P. J. Morrison, Phys. Fluids B **4**, 845 (1992).
[21]J. F. Drake and Y. C. Lee, Phys. Fluids **20**, 134 (1977).
[22]S. I. Braginskii, Rev. Plasma Phys. **1**, 205 (1965).
[23]H. R. Strauss, J. Comput. Phys. **28**, 437 (1978).
[24]P. L. Pritchett, Y. C. Lee, and J. F. Drake, Phys. Fluids **23**, 1368 (1980).
[25]C. Hildago, J. H. Harris, T. Uckan, J. D. Bell, B. A. Carreras, J. L. Dunlap, G. R. Dyer, C. P. Ritz, A. J. Wotton, M. A. Meier, T. L. Rhodes, and K. Carter, Nucl. Fusion **31**, 1471 (1991).
[26]R. J. Groebner, K. H. Burrell, and R. P. Seraydarian, Phys. Rev. Lett. **64**, 3015 (1990).
[27]H. Y. W. Tsui, H. Lin, M. Meier, C. Ritz, and A. J. Wotton, in *Proceedings of the 18th European Conference on Controlled Fusion and Plasma Physics*, Berlin (European Physical Society, Geneva, 1991), Vol. 15C, Part I, p. 297.
[28]E. R. Priest, *Solar Flare Magnetohydrodynamics* (Gordon and Breach, New York, 1981), Chap. 5.
[29]P. Sturrock, *Solar Flares* (Colorado Associated University Press, Boulder, CO, 1980), pp. 83–117.